

# 6G RIS in Indoor Environments: Assessment of Exposure Variability in Human Users and Non-Users

SILVIA GALLUCCI<sup>1</sup>, MARTINA BENINI<sup>1</sup>, SERENA FIOCCHI<sup>1</sup>, GABRIELLA TOGNOLA<sup>1</sup>, AND MARTA PARAZZINI<sup>1</sup>, MEMBER, IEEE

<sup>1</sup> Istituto di Elettronica e di Ingegneria dell'Informazione e delle Telecomunicazioni (IEIIT), Consiglio Nazionale delle Ricerche (CNR), 20133 Milan, Italy

CORRESPONDING AUTHOR: Silvia Gallucci (silvia.gallucci@cnr.it).

This work was supported by the European Union - Next Generation EU under the Italian National Recovery and Resilience Plan (NRRP), Mission 4, Component 2, Investment 1.3, CUP B53C22003970001, partnership on "Telecommunications of the Future" (PE00000001 - program "RESTART").

**ABSTRACT** The aim of the present work is to assess the exposure of human users and non-users in indoor scenarios due to novel technology that will be integrated in 6G network in order to overcome the obstacles in NLOS area: Reconfigurable Intelligent Surface (RIS), here tuned in FR1-band. The exposure assessment was conducted in two simplified indoor scenarios, single room and office, where the transmission angle of the RIS were varied mimicking the RIS following the user, and the Specific Absorption Rate (whole-body and brain SAR) were calculated. Five human models from Virtual Population (ViP) were considered differing between each other for anatomical characteristics.  $SAR_{wb}$  and  $SAR_{brain}$  results, studied in terms of peak values, cumulative distribution functions (CDFs) and spatial maps, showed higher  $SAR_{wb}$  values in adults compared to children, while  $SAR_{brain}$  peaks were more pronounced in child models. The study also revealed that there are few cases in which the exposure of non-user could be higher than the user. Moreover, the CDFs demonstrated that, for all the considered models, the probability that very low  $SAR_{brain}$  and  $SAR_{wb}$  levels occur is noticeably high. However, in general all the results are well below the ICNIRP Guidelines limits.

**INDEX TERMS** 6G, exposure assessment, Reconfigurable Intelligent Surface, ray tracing

## I. INTRODUCTION

In the wake of the continuous technological progress, the demand for even better performance of communication, both in terms of data rate and the amount of information exchanged, is continuously increasing and it recently opened up the prospect of Sixth Generation (6G) connections. The 6G technology will provide the realization of the Internet of Everything (IoE) theory where a wide number of items of a common scenario is equipped with a system able to transmit and receive massive amount of data [1], e.g. from wearable devices and implantable sensors at low-level, up to vehicles, train, industrial robot at very high-level. This concept will make possible many futuristic applications, such as virtual/augmented reality, brain-computer/machine interface, connected autonomous vehicles, connected health, and indoor localization [2]. From the technical point of view, all these applications mainly need high data rate requirement, and this

is guaranteed by mmWaves band (30-300 GHz) and THz band defined in the range (0.1-10) THz, with a reached data rate of 1Tb/s and latency of (10-100)  $\mu$ s [3]. Moreover, 6G communication networks will provide a pervasive connectivity and this means that typical communication scenarios (e.g., home Wi-Fi networks, control system in factories, wearable devices networks [4]) will completely change and will be re-defined as Smart Environment in which the environment will no longer host the network but will itself be part of the network becoming a reconfigurable surface that actively participates in transferring and processing information [5]. This implies that all environments in which 6G technology as a whole is used, can be defined as "smart", thus giving rise to "smart cities", "smart buildings", "smart university campuses", "smart factories", "smart homes" and

so on [6].

Unfortunately, 6G communications are prone to a remarkable path loss whereby it is not easily possible to exchange information between the elements belonging to the same 6G network, and a common obstacle can degrade the quality of service (QoS) [7]. In order to surpass this strong limit, the environment becomes useful to control the electromagnetic field (EMF) propagation, and this is feasible by acting on the scatterers, both in outdoor and in indoor scenarios [8]. This objective could be achieved by means of metasurfaces, that are surfaces made of metamaterial able to force beam direction in the desired one to optimize the transmission of the signal [9]. This is an effective way to include the environment in the network with the aim to enhance the quality of communications. In this perspective, the Reconfigurable Intelligent Surface (RIS) appears to be a promising candidate as they are able to steer the EMF towards the target in a programmable and controllable way [10]. In fact, the recently developed RIS is made up of a large number of elements that are configured as a whole to achieve beamforming with controllable intensity and direction [11]. Among various purposes for which the RIS can be employed, such as alternatives for infrared array sensors for positioning/localization [12], high performance wireless power transfer [13], or assistance for vital signal detection [14], this specific 'electromagnetic mirror' capability is very exploitable in environments in which there are many elements creating obstacles to the propagation of the EMF. Indeed RIS can overcome the limit of Non-Line-of-Sight (NLOS) due to such obstacles by creating virtual Line-of-Sight (LOS) able to direct the signal to the target via an alternative path [4]. This NLOS factor is present as much in outdoor scenarios where the obstacles are, for example, buildings as in indoor scenarios where instead walls dividing rooms can obstacle the communication between the Base Station (BS) and the device [15], [16]. Moreover, the RIS must be easily integrated in the network, so the dedicated frequency bands range from FR1-sub6GHz band (410-7125 MHz), FR2-mmWaves band (24.25-71 GHz), and THz band [9].

With the introduction of RIS, the environment becomes "smart", but this transformation implies that the scenario changes in terms of EMF propagation, considering that the electromagnetic signal will be transmitted in custom manner to optimize its power and improve the network coverage. As a consequence, also the exposure to the environmental EMF will be different for human users and non-users moving into such surroundings. At the best of our knowledge, in literature little has been done so far to assess the human exposure in such type of environments. Until now, indeed, the human exposure has been marginally evaluated and seen only as a user-constraint to be considered in network planning and optimization in some specific network configuration [10], [17], [18]. However, in literature there are not exhaustive studies in which the focus is on the exposure of both user and non-user in typical environments due to these new devices

impacting on the distribution of the electromagnetic field in the space.

In light of these considerations, the present study aims to fill this gap of knowledge. More specifically, this paper addresses the human exposure assessment in typical daily life environments equipped with RIS. For this purpose, we simulated a RIS placed in two indoor scenarios, a room and an office, composed of three identical and communicating rooms. The RIS was modelled as FR1, tuned to 5 GHz, and placed in the upper part of the walls.

The first step of the present study was to estimate the electric field ( $E$ , V/m) from an active RIS in the two scenarios and this was achieved by the employment of a ray tracing method. This phase was propaedeutic to the second step in which the exposure was quantified by the estimation of Specific Absorption Rate (SAR, W/kg) that is the amount of EMF power absorbed per unit mass of body tissue. The relevance of the SAR as exposure metrics is highlighted by the fact that it is the quantity with which the International Commission on Non-Ionizing Radiation Protection (ICNIRP) Guidelines [19] defines exposure limits for EMF sources tuned up to 6 GHz, so making the SAR the standard exposure metrics for the here considered scenarios. More specifically, here the whole-body SAR ( $SAR_{wb}$ , W/kg) and the brain SAR ( $SAR_{brain}$ , W/kg) were evaluated. Moreover, the estimation of these two exposure quantities were performed hypothesizing the presence in the studied environments of several human beings, differing between each other for physical characteristics in order to include in the study the element of the variability owing to human bodies that differ between each other for age and gender. The exposure assessment was performed for both user and non-users, where the term 'user' refers to the subject towards which there is the link between the RIS and the user equipment, while the 'non-users' are the other subjects that can be everywhere in the indoor scenarios.

## II. MATERIAL AND METHODS

### A. INDOOR SIMULATED SCENARIOS

In order to perform an exposure assessment study in typical settings of applications of RISs, two different simplified indoor scenarios were simulated. Both the environments were modelled using the 3D modelling software Blender (v. 4.2.1, Stichting Blender Foundation, Amsterdam).

Fig. 1A shows the first scenario (*Scenario A*) that is an empty room with size  $3 \times 3 \times 2.7 \text{ m}^3$ , representative of a possible scenario in which the RIS is employed for positioning or localization. The RIS was placed in the upper part of the left perimeter wall at the height of 2.4 m from the ground. Fig. 1B reports the more complex scenario (*Scenario B*): an office made of three rooms modelled as three identical modules connected through openings, simulating open doors ( $0.8 \times 2.1 \text{ m}$ ). Here, the RIS was placed in the middle room at the height of 2.4 m so it can transmit to and receive from both the other

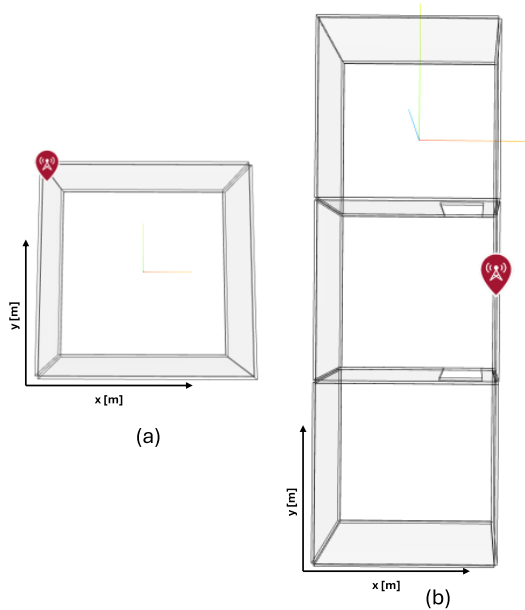


**FIGURE 1.** Simulated scenarios representing typical indoor way of use of RIS. (a) *Scenario A* constituted by a single room with the RIS in the upper left angle of the room at 2.4 m of height. (b) *Scenario B* made of three identical rooms with the RIS placed at the center of the middle one at 2.4 m from the ground. The transmit point (RIS) is represented as a red mark.

rooms. In *Scenario B* the RIS is intended to be used as a “electromagnetic mirror” with the presence of obstacles.

It is essential to point out that, in this study, the source generating the EMF reflected by the RIS was not modeled, since the aim of the study was to assess the exposure for both users and non-users in the whole environment only due to the introduction of RIS in the pre-existing indoor communication network, thus focusing on the specific contribution that the use of the RIS would have to the exposure.

The RIS was modeled as a MIMO with a 10-by-10 planar rectangular array of uniform interelement spacing of half-wavelength ( $\lambda/2$ ) with a resonant frequency of 5 GHz, belonging to the FR1 band and a transmitted power of 0.1 W, which corresponds to the limit of 20 dBm in indoor applications [20]. Furthermore, in order to represent in the simulation the capability of the RIS to modify the transmission angle so as to optimize the communication, the study was carried out for different transmission angles along the azimuth direction whereas the elevation angle is fixed. Specifically, the beam emitted by the RIS is always tilted by  $30^\circ$  in order to expose to the main lobe of the EMF provided by the RIS all the human models considered in this study and described in the following section, having different heights. As to the azimuth direction, in *Scenario A*, three transmission angles were considered with a difference of  $30^\circ$  between each successive angle (Angle 1A (i.e.,  $0^\circ$ ), Angle 2A (i.e.,  $30^\circ$ ), angle 3A (i.e.,  $60^\circ$ ) of Fig. 2A). In *Scenario B*, four angles were analyzed: three angles allowing the transmission in one of the adjacent rooms (*Room 1*) through the door, with a difference of  $10^\circ$  between them (i.e., Angle 2B (i.e.,  $102^\circ$ ), Angle 3B (i.e.,  $112^\circ$ ), and Angle 4B (i.e.,  $122^\circ$ ) of Fig 2B), and the  $0^\circ$  angle, corresponding to a transmission in the same

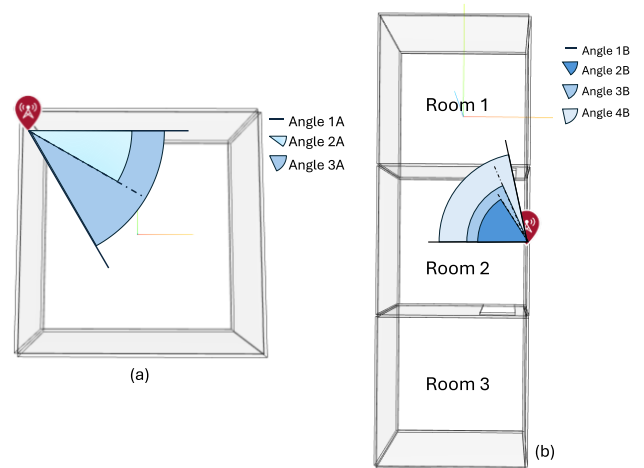


**FIGURE 2.** Scenarios representing typical indoor way of use of RIS where the transmission angles are reported. (a) *Scenario A* with Angle 1A ( $0^\circ$ ), Angle 2A ( $30^\circ$ ), Angle 3A ( $60^\circ$ ). (b) *Scenario B* with Angle 1B ( $0^\circ$ ), Angle 2B ( $102^\circ$ ), Angle 3B ( $112^\circ$ ), and Angle 4B ( $122^\circ$ ). The angles are represented in scale of blue. The transmit point (RIS) is represented as a red mark.

room where the RIS is placed (*Room 2*) (Angle 1B (i.e.,  $0^\circ$ ) of Fig. 2B). The different transmission angles were realized thanks to the phase shift that was varied according to the desired direction of the beam, starting from a phase shift of  $0^\circ$  for Angles 1A and 1B. In *Scenario B* the transmission angles were defined aiming the optimal EMF transmission through the door and towards the room in which the receiver (i.e. the user) is supposed to be placed. Moreover, in both scenarios, all the rooms are empty, thus the walls are the only obstacle to the communication with their width of 10 cm.

## B. RAY TRACING METHOD FOR E FIELD CALCULATION

The exposure metric calculated in the present study and chose according to the international guidelines [19] is the Specific Absorption Rate (SAR, W/kg) for the whole- and the brain. More in details, the first step to calculate them was the estimation of the electric field (E, V/m) in all the studied environments. This quantity was obtained by means of the raytracing method implemented in MATLAB R2024a (www.mathworks.com). More specifically, a multipath propagation model was used to determine propagation paths and their associated path losses. The raytracing analysis was performed with the Shooting and Bouncing Rays (SBR) method [21] where effects from surface reflections are included but not the effects from corner diffraction, refraction or rough-surface diffuse scattering. Then, in this study, the number of reflections was set equal to 6 and the ray spacing was set as “medium” (approximately  $0.54^\circ$ ). Finally, the walls belonging to the scenarios were characterized through the dielectric properties of the concrete ( $\epsilon_r = 5.24$ ,  $\sigma = 0.0548$  S/m) (www.mathworks.com). The E field was estimated in the whole space thanks to 225 receivers (i.e., grid points in which the electric field is evaluated) in *Scenario A* and 690 receivers in *Scenario B* uniformly placed on a grid of 0.2 m step along the x and y directions and at fixed heights along the z direction.

These receivers mimic the position of the human model inside the studied environments. Indeed, E was calculated at those heights that correspond to the height of the head and the brain of the considered human models. The final obtained results of the ray-tracing step were the spatial distributions of the electric field at the heights of interest in order to estimate, in the next step, the SAR<sub>wb</sub> and the SAR<sub>brain</sub>.

### C. HUMAN MODELS AND SAR ESTIMATION

SAR was assessed in five human models of the Virtual Population (ViP) [22] of both genders and age in the range 3-34 years. The whole-body SAR (SAR<sub>wb</sub>), and the brain SAR (SAR<sub>brain</sub>), were calculated according to the following formulas, valid for far-field exposure conditions [23]:

$$SAR_{brain}(f) = (E_{inc}/E_{ref})^2 * SAR_{brain-FDTD}(f) \quad (1)$$

$$SAR_{wb}(f) = (E_{inc}/E_{ref})^2 * (BMI_{ref-model}/BMI) * SAR_{wb-FDTD}(f) \quad (2)$$

In Equation (1) and Equation (2), E<sub>inc</sub> (V/m) is the incident electric field calculated in the present study via raytracing in each scenario. The E field was calculated at two different heights: at the ‘head’ height, for the calculation of the SAR<sub>wb</sub>, and at 2 cm under the height of the human model for the SAR<sub>brain</sub> (e.g., brain height of Nina is 0.90 cm). The (1) and (2) formulas were obtained in far-field conditions where human models of the Virtual Population (ViP) [22], referred in (2) as ‘ref-model’, were hit by a specific set of plane waves in which the amplitude of the incident electric field (E<sub>ref</sub>, V/m) is equal to 2.45 V/m. SAR<sub>wb-FDTD</sub> and SAR<sub>brain-FDTD</sub> values are specified in Table II and they have to be set according to the frequency of the EMF source, up to 5.8 GHz. The described quantities were derived by the computational study in [23] based on the FDTD numerical method applied on the reference model, whose BMI<sub>ref-model</sub> (kg/m<sup>3</sup>) is its Body-Mass Index, whereas BMI (kg/m<sup>3</sup>) is the one of the models employed in the present study and, in this specific case, they coincide.

The SAR<sub>brain-FDTD</sub> and SAR<sub>wb-FDTD</sub> values provided by [23] were calculated not exactly at 5 GHz but at 5.2 GHz. However, for 5 GHz, the dielectric properties of human tissues [24], [25] were strongly similar to those reported at 5.2 GHz and, for this reason, in the present work that coefficients were employed.

**TABLE 1. Anatomical characteristics of the analyzed members of the ViP**

Model	Age (y.o.)	Weight (kg)	Height (m)	BMI (kg/m <sup>3</sup> )
Duke	34	70.2	1.77	22.4
Ella	26	57.3	1.63	21.6
Billie	11	34	1.49	15.3
Thelonius	6	18.6	1.16	13.8
Nina	3	13.9	0.92	16.4

### D. DATA ANALYSES

The calculated SAR<sub>wb</sub> and SAR<sub>brain</sub> values were analyzed to assess (i) the maximum exposure values in all the realistic

simulated scenarios, (ii) the probability for a subject to be exposed in a more or less complex environment to specific

**TABLE 2. SAR<sub>wb-FDTD</sub> and SAR<sub>brain-FDTD</sub> values of the human models investigated [21]**

Model	SAR <sub>wb-FDTD</sub> (W/kg)	SAR <sub>brain-FDTD</sub> (W/kg)
Duke	$3.7 \times 10^{-5}$	$3.6 \times 10^{-6}$
Ella	$4 \times 10^{-5}$	$7.7 \times 10^{-6}$
Billie	$5.3 \times 10^{-5}$	$1.5 \times 10^{-5}$
Thelonius	$6.9 \times 10^{-5}$	$2.3 \times 10^{-5}$
Nina	$6 \times 10^{-6}$	$7.8 \times 10^{-7}$

SAR values and, (iii) the spatial distribution of the SAR, thus the area of the scenario in which the human being could be more exposed to the EMF emitted by the RIS. Thanks to this last analysis, it was also possible to differentiate the user and non-user exposure conditions since from these maps it is possible to detect the direction of the beam from the RIS, that is the one towards the user.

In more technical terms, the analyzed parameters were: (i) the spatial peaks of SAR<sub>wb</sub> and SAR<sub>brain</sub> for both simulated scenarios, across all considered human models to assess the maximum dose absorbed. (ii) the Cumulative distribution functions (CDFs) of SAR<sub>wb</sub> and SAR<sub>brain</sub>, to determine the probability that SAR<sub>wb</sub> and SAR<sub>brain</sub> values, respectively, are less than or equal to a fixed threshold that is, in this work, the peak SAR reduced by 3 dB (approximately half of its value) and referred to from now on as SAR<sub>3dB</sub>. CDFs are calculated starting from all the data obtained for each transmission angle of the RIS, (i) for the entire *Scenario A* in which a single room is represented, (ii) exclusively for *Room 1* in *Scenario B*, that is the room adjacent to the one where the RIS is placed and where the EMF is directed. The choice to compare the CDFs of the data of the entire *Scenario A* with those of only *Room 1* of *Scenario B* is due to intention to ensure a balanced analysis between two different set of data obtained from two distinct scenarios. (iii) Spatial mapping of SAR<sub>wb</sub> and SAR<sub>brain</sub> peak values across *Scenario B* comprising all the three rooms. The SAR<sub>wb</sub> and SAR<sub>brain</sub> data represented in these maps are, in each point of the evaluation grid in the rooms, the maximum values among the three transmission angles. Moreover, these spatial distributions were characterized by calculating their Kurtosis and the Coefficients of Variations (CVs).

Lastly, the compliance of the obtained SAR peaks with the ICNIRP Guidelines [19] limits was also checked.

## III. RESULTS

### A. SCENARIO A

The upper panels of Figure 3 and of Figure 4 display respectively the peaks of SAR<sub>wb</sub> and SAR<sub>brain</sub> for a subject positioned at each grid point in the room, for all the human models included in the study.

Both panels indicate that peak SAR values, valid for both users and non-users, calculated for beam angles Angle 2A (i.e., 30°) and Angle 3A (i.e., 60°) are nearly identical across all studied human models. In contrast, Angle 1A (i.e., 0°) exhibits a distinct pattern, with peak SAR values significantly higher.

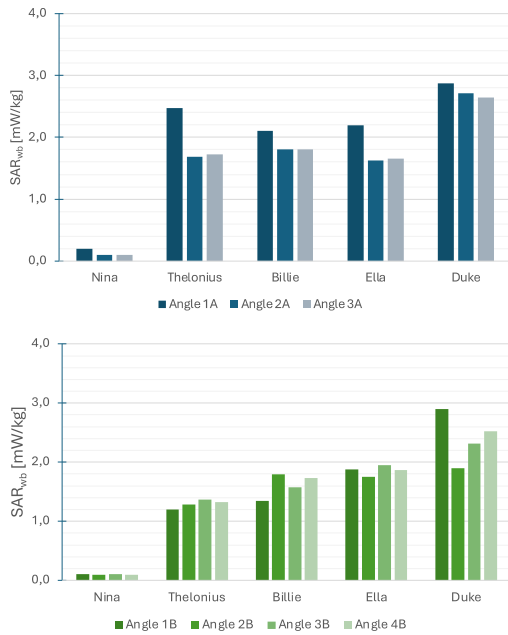


**FIGURE 3.** Peak values of SAR<sub>wb</sub> obtained in the two simulated scenarios with all the transmission angles and five human models. Upper panel refers to SAR<sub>wb</sub> obtained in Scenario A whereas the bottom panel to the ones obtained in Scenario B.

Specifically, the highest SAR<sub>wb</sub> is observed in Duke (i.e., 2.9 mW/kg) with RIS oriented according to Angle 1A, while the highest SAR<sub>brain</sub> is found in Thelonus (i.e., 0.83 mW/kg), again at Angle 1A. This means that, in Scenario A, the worst case has Angle 1A as transmission angle of the RIS. The main reason for the finding in this specific scenario is that, without phase shift to focalize the beam at a specific azimuth angle, most of the power is concentrated in the main beam (i.e., scenario with Angle 1A), otherwise it is also distributed in the side beams arising due to the phase shift, the condition that occurs in the other two cases, i.e., Angle 2A and Angle 3A. Moreover, both panels clearly demonstrate that Nina, the youngest, lightest and shortest model, consistently reports the lowest values for both SAR<sub>wb</sub> and SAR<sub>brain</sub>.

Figure 5 shows the CDF of SAR<sub>wb</sub> and SAR<sub>brain</sub> calculated in the room for each individual model. Since most of the SAR data are strongly concentrated around zero values, all the CDFs could be approximated by Gamma distributions, therefore the trend of the curves is always the same. Moreover, the probability of SAR<sub>wb</sub> values being lower than the SAR<sub>-3dB</sub> in Scenario A is consistently greater than 90%, indicating that the exposure levels in the room are generally very low with a very localized peak. This means that only the user or the non-user positioned along the beam is exposed to the highest values, while all the other non-users (i.e. the subjects positioned elsewhere in the room) experienced very low SAR<sub>wb</sub> values.

Moreover, from the graphs it is clear that the shapes of the curves are highly similar across all considered angles. The only exception is the curve of the CDF of Nina (i.e., light blue

line), which differs from the others for all transmission angles of interest, exhibiting the steepest slope.

Focusing on the bottom row relative to the CDFs obtained from SAR<sub>brain</sub> values, the trend of very low values is evident as much as from the SAR<sub>wb</sub> values, and in this case the probability to find in Scenario A SAR<sub>brain</sub> values lower than its SAR<sub>-3dB</sub> is 99%. In general, this observation is confirmed in all the panels by considering that the probability to have almost null SAR values is, at least, 38%.

### B. SCENARIO B

The bottom panel of Figure 3 and of Figure 4 displays respectively the peaks of SAR<sub>wb</sub> and SAR<sub>brain</sub> for the whole Scenario B, including the three rooms where the subject is positioned. The lowest SAR<sub>wb</sub> is consistently found in Nina, independent of the transmission angle, whereas the highest SAR<sub>wb</sub> is observed in Duke model at a transmission angle 1B (i.e., 0°), with a value of 2.9 mW/kg, similar to Scenario A. Additionally, this result confirms the findings obtained in Scenario A also in terms of transmission angle with the tallest human model, where the beam with an angle of 0° (i.e., scenario with Angle 1B) gave the highest SAR<sub>wb</sub> and SAR<sub>brain</sub> values.

Furthermore, when comparing exposure levels excluding the peaks associated with Angle 1B, observing one single human model at a time, it is clear that there is no systematic relation between the peaks extracted in the various angles. In fact, the maximum deviation between the SAR<sub>wb</sub> peaks within each single model ranges from 4% in Nina up to 34% in Duke. This variability is mirrored in the SAR<sub>brain</sub> values, where the maximum deviation reaches 19.9% in Ella and decreases to 3.7% in Nina.

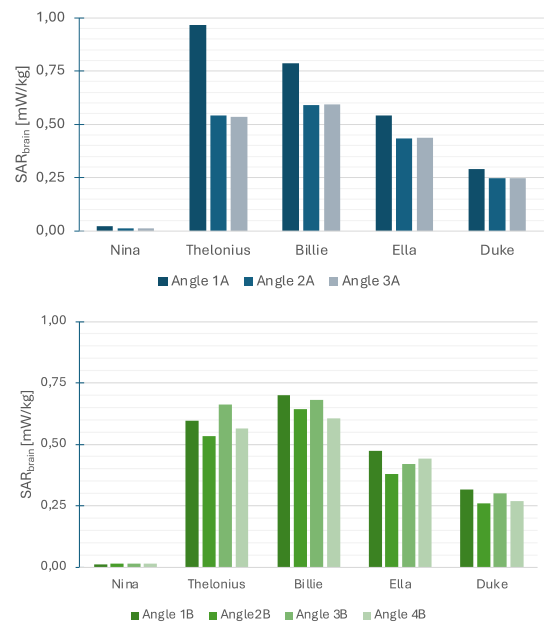


**FIGURE 4.** Peak values of SAR<sub>brain</sub> obtained in the two simulated scenarios for all the four analyzed transmission angles and the five human models. The upper panel refers to SAR<sub>brain</sub> obtained in Scenario A whereas the bottom panel to the ones obtained in Scenario B.

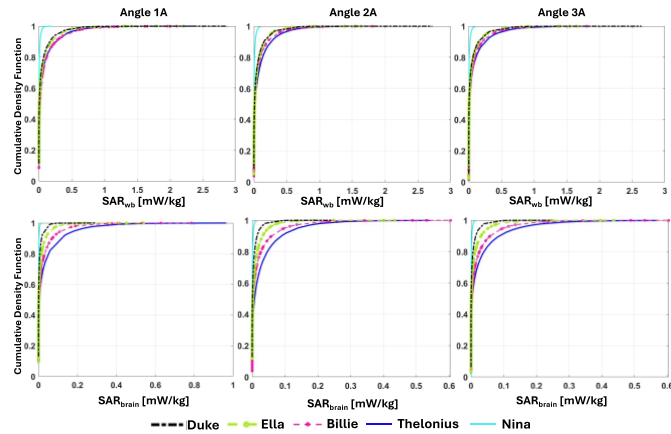


**FIGURE 5.** Cumulative density functions of the  $SAR_{wb}$  (upper panels) and  $SAR_{brain}$  (bottom panels) distributions collected in *Scenario A*. The data were divided according to the transmission angle of the RIS. In each graph, the data relative to the five human models considered are reported.

Bottom panel of Fig. 4 further demonstrates that the highest  $SAR_{brain}$  is recorded in the Billie model at a transmission angle 1B, with a value of 0.7 mW/kg, and remains the highest one across all transmission angles. Besides, as in previous cases, the lowest  $SAR_{brain}$  values are observed in Nina model, with exposure levels of 0.01 mW/kg.

Figure 6 presents the cumulative distribution functions (CDFs) of whole-body SAR ( $SAR_{wb}$ ) in the upper panels and brain-specific SAR ( $SAR_{brain}$ ) in the lower panels and it refers only to the SAR values detected in *Room 1* of the office simulated through the *Scenario B*. Generally, the  $SAR_{wb}$  CDFs for the adult male model (Duke) and the female child model (Nina) exhibit similar trends. This indicates that the shortest and tallest models have a lower probability of experiencing high  $SAR_{wb}$  values in this room. Concerning Duke, this finding may be due to the ratio between the height of Duke and his distance from the source, whereas the peaks in Nina are always the lowest ones, so the related CDF is positioned towards very low values of SAR and quickly reaching the maximum of the CDF, 1.

Conversely, the CDF derived from the male child model (Thelonius) shows a distinct pattern, showing the lowest

**TABLE 3.** Coefficients of Variation (CV) and kurtosis of  $SAR_{wb}$  and  $SAR_{brain}$  distributions on the studied human models in *Scenario B*

Model	Duke	Ella	Billie	Thelonius	Nina
<i>Kurtosis</i>	67.5	52	35.7	20.2	16.1
<i>CV</i> $SAR_{wb}$	6.1	4.9	4.2	3.2	2.8
<i>Kurtosis</i>	87.9	59.9	47.9	26.2	17.1
<i>CV</i> $SAR_{brain}$	6.6	5.4	4.7	3.5	2.9

probability of experiencing small  $SAR_{wb}$  values, followed by the female pre-teenager model (Billie). Furthermore, the graphs confirm that the probability of  $SAR_{wb}$  values being equal to or lower than its  $SAR_{3dB}$  consistently exceeds 95%. This finding suggests again a general tendency toward very low  $SAR_{wb}$  values with a uniform spatial distribution, except

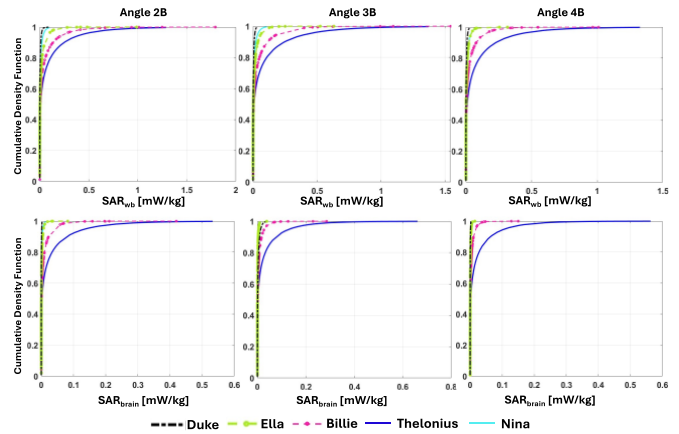


**FIGURE 6.** Cumulative density functions of the  $SAR_{wb}$  (upper panels) and  $SAR_{brain}$  (bottom panels) distributions collected in *Scenario B*. The data were divided according to the transmission angle of the RIS. In each graph, the data relative to the five human models considered are reported.

in areas where the EMF beam is concentrated (i.e. where the user is posed) due to the beamforming effect implemented by the RIS. Moreover, these observations remain valid for all the three transmission angles configurations. Similar considerations can be made for the  $SAR_{brain}$  CDFs.

Figures 7 and 8 depict the spatial mapping in the whole environment in *Scenario B* of peak  $SAR_{wb}$  and  $SAR_{brain}$  values deriving from the three transmission angles directed towards *Room 1*, respectively. These maps provide a comprehensive overview of the environmental distribution of SAR. For clarity, most part of the discussion that follows focuses on the  $SAR_{wb}$  maps; however, the observations are equally applicable to  $SAR_{brain}$ .

The maps uniformly show that the regions affected by the EMF emitted by the RIS, and consequently the absorbed dose, are seen along the direction in which the beam is focalized, as expected. The influence of beamforming is clearly evident, with SAR levels being essentially null in *Room 3*, where no significant radiation is observed. Moreover, it is evident that not all SAR peaks are in *Room 1*, and this means that potentially a non-user in *Room 2* could be more exposed than the user in *Room 1* where the beam is directed.

In relation to the human models, panels illustrate that SAR distributions vary depending on the specific model. Notably, adult models exhibit distributions that are less uniform and skewed toward higher values, whereas preadolescent and child models demonstrate distributions concentrated around lower values. Kurtosis and coefficients of variations (CV) collected in Table III confirm these observations with the kurtosis highest value for the data from Duke, and the less one in the female child model, Nina. Regarding data variability, the CVs reveal slightly greater variability in  $SAR_{brain}$  compared to  $SAR_{wb}$ , and that the maximum value of CV is still found in Duke as well as the lowest one is obtained in Nina, consistently with the kurtosis values.

#### IV. DISCUSSION

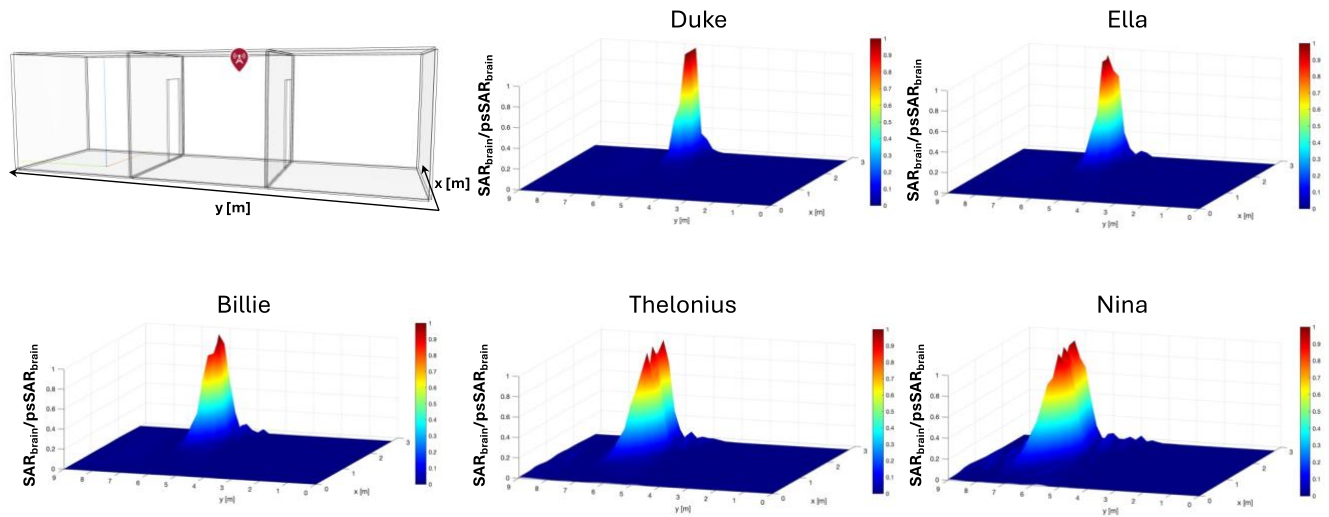


**FIGURE 7.** Spatial distribution of the  $SAR_{brain}$  in the whole *Scenario B*. The maps represent the maximum values of  $SAR_{brain}$  obtained with the three transmission angles directed towards *Room 1* (i.e., Angle 2B, 3B, and 4B). In each graphs the scales are different, and each one is referred to the maximum of the respective spatial map. All the results are normalized with respect to the maximum of each distribution.

The present work is, to the best of our knowledge, the first study that estimated human exposure due to new 6G technologies in an indoor scenario in which a characterizing element is inserted: Reconfigurable Intelligent Surface (RIS). The presence of such device completely changes the environmental distribution of the EMF emitted by the already set network in daily places since the RIS is also conceived to overcome the limit due to the environmental obstacles by eluding them, both in indoor and outdoor scenarios. For this reason, it is reasonable to hypothesize that the exposure of human beings living in such places is modified and thus the need to investigate the consequent changes is arising. Here, the spatial distributions of the exposure metrics ( $SAR_{wb}$  and  $SAR_{brain}$ ) were obtained after the estimation of the environmental electric field levels through the raytracing method. These spatial distributions were calculated for several transmission angles of the RIS. These results were necessary to achieve the spatial maps of the SAR to know punctually in the space the entity of the EMF power absorbed by human users and non-users. Besides, this whole work was performed for two typical scenarios (i.e., room and office) and the exposure quantities, i.e.,  $SAR_{wb}$  and  $SAR_{brain}$ , were estimated for five human models, differing between each other for their anatomical characteristics, including two adult (male and female), one pre-teenager and two child models (male and female).

The present study revealed that in terms of the only EMF contribution due to the RIS, from the comparison between the presented peak values of  $SAR_{wb}$  and the ICNIRP Guidelines basic restrictions [19], that is 0.4 W/kg for the frequency of interest, the peak values here obtained never exceed the international limit. Indeed the highest value of  $SAR_{wb}$  obtained in Duke model is more than two order of magnitude less than the ICNIRP Guidelines limit. Moreover, in literature there are works (e.g. [20], [26], [27]) in which many different environmental exposure conditions were studied, with EMF

sources more or less innovative, concluding that the exposure levels are always well below the international exposure limits [19]. By merging our findings with the literature ones, it may be affirmed that the exposure levels induced in a futuristic indoor scenario, where the newest and the previous sources are contemporary employed, do not exceed the dosimetric international limits. Indeed, comparing the results with the cumulative formula reported in ICNIRP Guidelines where the exposure due to multiple contemporary sources is quantified by the sum of the ratios between the SARs induced by EMF sources and the whole-body average SAR basic restrictions at each specific frequency, it is reasonable to affirm that the contribution given by our data in the totality of the exposure due to the other sources in the scenario is strongly limited since it is two orders of magnitude below the international limit. Another interesting result is related to the localization of the founded peaks since they always are in correspondence of the main lobe of the beam due to the RIS and this is consistent with the fact that this is the direction of the highest power as it is the favorite direction towards the user's equipment. This also means that the exposure of non-users possibly present in the environment is strongly less than of user, as expected because of the beamforming effect, except for the case in which the non-user is on the trajectory linking the RIS with the user, the only situation in which it is possible that the non-user exposure could be higher than the user one. Finally, no common trend was found in both scenarios regarding exposure levels as the transmission angles, and thus the phase shift, changed. This can be explained by the fact that the factors affecting exposure are both related to the scenario itself and how the RIS interacts with it, as well as EMF to SAR calculation factors.

Afterwards, the analyses were focused on the effects of the variability of the human subject exposed to the EMF due to the RIS since the use of various human models allows for a comprehensive comparison of  $SAR_{wb}$  and  $SAR_{brain}$  values

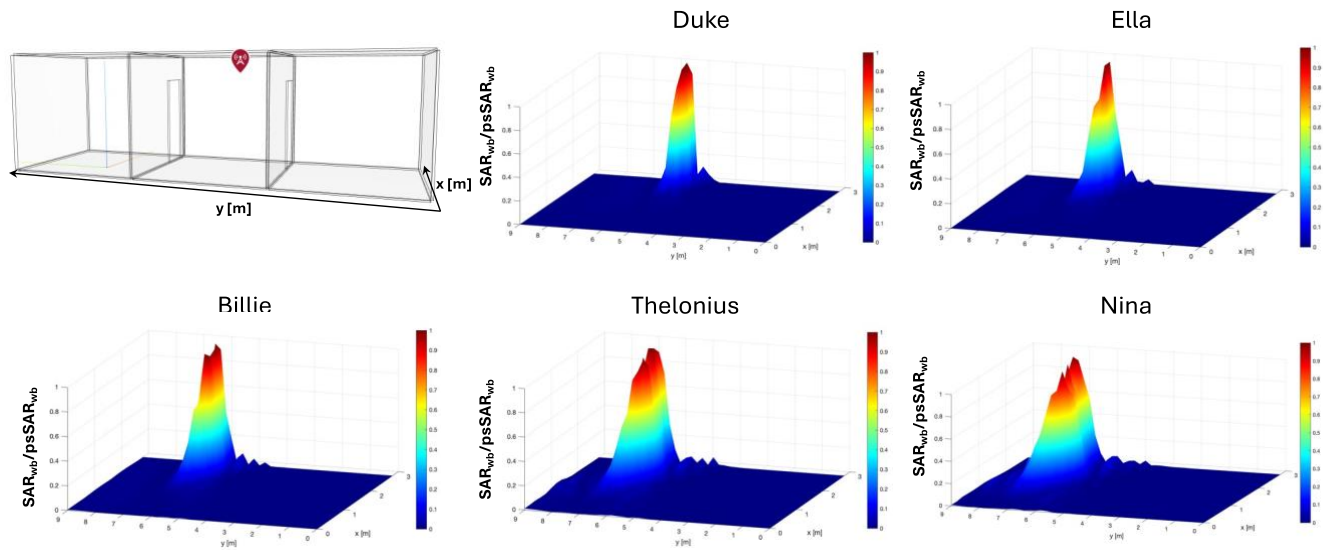


**FIGURE 8.** Spatial distribution of the  $SAR_{wb}$  in the whole *Scenario B*. The maps represent the maximum values of  $SAR_{wb}$  obtained with the three transmission angles directed towards *Room 1* (i.e., Angle 2B, 3B, and 4B). In each graphs the scales are different, and each one is referred to the maximum of the respective spatial map. All the results are normalized with respect to the maximum of each distribution.

calculated for each case. This analysis revealed that exposure levels are influenced by individual anatomical differences, which are observable in terms of peak values, cumulative distribution functions, and spatial mapping of the maximum. Specifically, peak  $SAR_{wb}$  values are higher in adult models compared to younger ones, whereas peaks  $SAR_{brain}$  are more evident in child models. Notably, this pattern is consistent across both scenarios. Focusing solely on the electric field and calculating for each model the distance at which the model intersects the main lobe emitted by the RIS, it is observed that the greater the height of the model, the shorter the distance between its position and the source. This implies that taller models are exposed to a stronger electric field due to the reduced distance from the source and the presence of side lobes. However, this trend is not reflected in SAR values, and the reason is mainly due to the coefficient in the Equation (1) and Equation (2). Indeed,  $SAR_{FDTD}$  coefficients are different depending on the human model. This fact is more appreciable in  $SAR_{brain}$  values, considering that the  $\Delta SAR_{brain-FDTD}$ , calculated as the difference between the highest and the lowest  $SAR_{brain-FDTD}$  across the different human model, is greater than the  $\Delta SAR_{wb-FDTD}$ , calculated accordingly.

In general, the study identified two factors as most influential on exposure levels: the height of the human model and its absorption characteristics. Indeed, the EMF power encountering the human being depends on the relationship between its height and its distance from the EMF emitter; moreover, the absorption characteristics including anatomical factors, such as the thicknesses of tissues depending on the model, are encompassed by the  $SAR_{FDTD}$  coefficients. A clear example of how these two factors affect SAR values is Nina, where the electric field is about 40% lower than in case of an adult model and  $SAR_{FDTD}$  coefficients are about one order of magnitude below the adult ones.

Concerning the probability analysis, different trends depending on the human model are not particularly noticeable through the CDFs; specifically, in *Scenario A*, the most evident divergent trend is of the female child model, whereas the other models present almost the same behavior. Conversely, the CDFs of  $SAR_{brain}$  revealed some differences in the slope of the curves whereby it can be concluded that the probability to find low values is greater in the adult models with respect to the younger ones. Once again, this is true for both the simulated scenarios. However, the CDFs of the SAR values calculated in *Scenario B* in some cases do not include the peak SAR. This suggests that the maximum value of the SAR is not reached in *Room 1* that is the one in which the beam is directed, but it is achieved in *Room 2*. This finding is consistent with the observations above regarding the peaks, indeed the delta between the actual SAR peak values and those represented in the CDFs increases with the height of the model. It is noteworthy the fact that these scenarios in which the peak SAR is not in the *Room 1* are examples of cases in which the exposure of a non-user in *Room 2* positioned along the trajectory of the beam may be higher than the exposure of a user in *Room 1*.

All these considerations found confirmation in the 3D spatial mapping in which it is clear that in Duke and Ella models the peak of both  $SAR_{wb}$  and  $SAR_{brain}$  are closer to the RIS with respect to the values calculated for Billie, Thelonius and Nina. Moreover, the spatial mapping also revealed that the distribution of the data is more uniform towards low values in case of the three young human models, while in case of Duke and Ella the peaks are more pronounced. This is confirmed by the kurtosis values showing that the distributions are increasingly flatter as human height decreases. The relation between the height of the human model and the behavior of the spatial distribution is confirmed by the CVs demonstrating

that the data from the shortest human models presented less variability than the data from the adult.

## V. CONCLUSIONS

In conclusion, the aim of the present work was to assess the human exposure in a future real-life scenario where RISs will be inserted as a novel technology able to make the 6G communication network more efficient. Here, only the exposure introduced by this novelty was considered in order to know the entity of its contribution to the EMF already present in an indoor environment. As a first study about the assessment of RIS-6G exposure, authors have simulated two simplified scenarios made of empty rooms, conscious of the fact that deepest characterization of the environment could slightly impact on the results. Moreover, in order to generalized more these findings, other frequency bands should be studied, since the interaction between EMF and biological tissues is frequency dependent.

The computational analysis conducted on five human models differing for anatomical characteristics in two indoor scenarios with several transmission angles of the RIS revealed that both the variability of the human model and that of the transmission angle impact on the exposure levels, here estimated starting from electric field values (the output of the implemented raytracing method), in the shape of  $SAR_{wb}$  and  $SAR_{brain}$ . In the studied scenarios, the highest exposure levels were always found in correspondence with the main lobe of the beam of the RIS since it is the direction towards the user's equipment, thus where the signal must be the strongest. This also means that there is the possibility that a non-user positioned along the link RIS-user's equipment may be more exposed than the user. Besides, the exposure due to the side lobes is very limited to low values and this implies that the environmental exposure is uniformly linked to low values of SAR, except for few peak values in the area covered by the main lobe, according with the radiation pattern of a beamformed source.

Furthermore, in terms of the impact of the human subject variability, this study has confirmed that the absorption of the EMF power by human tissues exhibit different behaviors depending on the specific human model considered. This is attributed to the physical characteristics of the human models, which are accounted for in the exposure metrics. Consequently, this study underscores the importance of conducting exposure assessment studies where specific parameters are calculated, particularly in innovative and futuristic scenarios, where the current scientific literature appears to be lacking.

## REFERENCES

- [1] S. Dang, O. Amin, B. Shihada, and M.-S. Alouini, "What should 6G be?," *Nat Electron*, vol. 3, no. 1, pp. 20–29, Jan. 2020, doi: 10.1038/s41928-019-0355-6.
- [2] B. Rana, S.-S. Cho, and I.-P. Hong, "Review Paper on Hardware of Reconfigurable Intelligent Surfaces," *IEEE Access*, vol. 11, pp. 29614–29634, 2023, doi: 10.1109/ACCESS.2023.3261547.
- [3] Y. Wu *et al.*, Eds., *6G Mobile Wireless Networks*. in Computer Communications and Networks. Cham: Springer International Publishing, 2021. doi: 10.1007/978-3-030-72777-2.
- [4] R. Chen, M. Liu, Y. Hui, N. Cheng, and J. Li, "Reconfigurable

- Intelligent Surfaces for 6G IoT Wireless Positioning: A Contemporary Survey," *IEEE Internet Things J.*, vol. 9, no. 23, pp. 23570–23582, Dec. 2022, doi: 10.1109/JIOT.2022.3203890.
- [5] M. D. Renzo *et al.*, "Smart radio environments empowered by reconfigurable AI meta-surfaces: an idea whose time has come," *J Wireless Com Network*, vol. 2019, no. 1, p. 129, Dec. 2019, doi: 10.1186/s13638-019-1438-9.
- [6] M. Di Renzo *et al.*, "Smart Radio Environments Empowered by Reconfigurable Intelligent Surfaces: How It Works, State of Research, and The Road Ahead," *IEEE J. Select. Areas Commun.*, vol. 38, no. 11, pp. 2450–2525, Nov. 2020, doi: 10.1109/JSAC.2020.3007211.
- [7] M. M. Amri, N. M. Tran, and K. W. Choi, "Reconfigurable Intelligent Surface-Aided Wireless Communications: Adaptive Beamforming and Experimental Validations," *IEEE Access*, vol. 9, pp. 147442–147457, 2021, doi: 10.1109/ACCESS.2021.3124319.
- [8] I. F. Akyildiz, A. Kak, and S. Nie, "6G and Beyond: The Future of Wireless Communications Systems," *IEEE Access*, vol. 8, pp. 133995–134030, 2020, doi: 10.1109/ACCESS.2020.3010896.
- [9] ETSI Industry Specification Group (ISG), "Reconfigurable Intelligent Surfaces (RIS); Use Cases, Deployment Scenarios and Requirements," ETSI GR RIS, 001 V1.1.1, 2023.
- [10] H. Ibraiwish, A. Elzanaty, Y. H. Al-Badarnah, and M.-S. Alouini, "EMF-Aware Cellular Networks in RIS-Assisted Environments," *IEEE Commun. Lett.*, vol. 26, no. 1, pp. 123–127, Jan. 2022, doi: 10.1109/LCOMM.2021.3120688.
- [11] X. Lei, M. Wu, F. Zhou, X. Tang, R. Q. Hu, and P. Fan, "Reconfigurable Intelligent Surface-Based Symbiotic Radio for 6G: Design, Challenges, and Opportunities," *IEEE Wireless Commun.*, vol. 28, no. 5, pp. 210–216, Oct. 2021, doi: 10.1109/MWC.121.2100126.
- [12] S. Hu, F. Rusek, and O. Edfors, "Beyond Massive MIMO: The Potential of Positioning With Large Intelligent Surfaces," *IEEE Trans. Signal Process.*, vol. 66, no. 7, pp. 1761–1774, Apr. 2018, doi: 10.1109/TSP.2018.2795547.
- [13] Y. Zheng, S. Bi, Y. J. Zhang, Z. Quan, and H. Wang, "Intelligent Reflecting Surface Enhanced User Cooperation in Wireless Powered Communication Networks," *IEEE Wireless Commun. Lett.*, vol. 9, no. 6, pp. 901–905, Jun. 2020, doi: 10.1109/LWC.2020.2974721.
- [14] J. U. R. Kazim *et al.*, "In-Home Monitoring Using Wireless on the Walls for Future HealthCare: Real-World Demonstration," *Advanced Intelligent Systems*, vol. 5, no. 9, p. 2300007, Sep. 2023, doi: 10.1002/aisy.202300007.
- [15] I. Yildirim, A. Uyrus, and E. Basar, "Modeling and Analysis of Reconfigurable Intelligent Surfaces for Indoor and Outdoor Applications in Future Wireless Networks," *IEEE Trans. Commun.*, vol. 69, no. 2, pp. 1290–1301, Feb. 2021, doi: 10.1109/TCOMM.2020.3035391.
- [16] M. Issa and H. Artail, "Using Reflective Intelligent Surfaces for Indoor Scenarios: Channel Modeling and RIS Placement," in *2021 17th International Conference on Wireless and Mobile Computing, Networking and Communications (WiMob)*, Bologna, Italy: IEEE, Oct. 2021, pp. 277–282. doi: 10.1109/WiMob52687.2021.9606297.
- [17] A. Zappone and M. D. Renzo, "Energy Efficiency Optimization of Reconfigurable Intelligent Surfaces With Electromagnetic Field Exposure Constraints," *IEEE Signal Process. Lett.*, vol. 29, pp. 1447–1451, 2022, doi: 10.1109/LSP.2022.3181532.
- [18] B. Yin, W. Joseph, and M. Deruyck, "RIS-Aided mmWave Network Planning Toward Connectivity Enhancement and Minimal Electromagnetic Field Exposure," *IEEE Access*, vol. 11, pp. 115911–115923, 2023, doi: 10.1109/ACCESS.2023.3325678.
- [19] ICNIRP, "Guidelines for Limiting Exposure to Electromagnetic Fields (100 kHz to 300 GHz)," *Health Physics*, vol. 118, no. 5, pp. 483–524, May 2020, doi: 10.1097/HP.0000000000001210.
- [20] E. Chiaromello *et al.*, "Innovative Stochastic Modeling of Residential Exposure to Radio Frequency Electromagnetic Field Sources," *IEEE J. Electromagn. RF Microw. Med. Biol.*, vol. 5, no. 1, pp. 62–69, Mar. 2021, doi: 10.1109/JERM.2020.2994560.
- [21] Z. Yun and M. F. Iskander, "Ray Tracing for Radio Propagation Modeling: Principles and Applications," *IEEE Access*, vol. 3, pp. 1089–1100, 2015, doi: 10.1109/ACCESS.2015.2453991.
- [22] M.-C. Gosselin *et al.*, "Development of a new generation of high-resolution anatomical models for medical device evaluation: the Virtual Population 3.0," *Phys. Med. Biol.*, vol. 59, no. 18, pp. 5287–5303, Sep. 2014, doi: 10.1088/0031-9155/59/18/5287.
- [23] I. Liorni *et al.*, "EVALUATION OF SPECIFIC ABSORPTION RATE IN THE FAR-FIELD, NEAR-TO-FAR FIELD AND NEAR-FIELD

REGIONS FOR INTEGRATIVE RADIOFREQUENCY EXPOSURE ASSESSMENT,” *Radiation Protection Dosimetry*, vol. 190, no. 4, pp. 459–472, Oct. 2020, doi: 10.1093/rpd/ncaa127.

[24] C. Gabriel, S. Gabriel, and E. Corthout, “The dielectric properties of biological tissues: I. Literature survey,” *Phys. Med. Biol.*, vol. 41, no. 11, pp. 2231–2249, Nov. 1996, doi: 10.1088/0031-9155/41/11/001.

[25] S. Gabriel, R. W. Lau, and C. Gabriel, “The dielectric properties of biological tissues: II. Measurements in the frequency range 10 Hz to 20 GHz,” *Phys. Med. Biol.*, vol. 41, no. 11, pp. 2251–2269, Nov. 1996, doi: 10.1088/0031-9155/41/11/002.

[26] M. Bonato *et al.*, “Human RF-EMF Exposure Assessment Due

to Access Point in Incoming 5G Indoor Scenario,” *IEEE J. Electromagn. RF Microw. Med. Biol.*, vol. 5, no. 3, pp. 269–276, Sep. 2021, doi: 10.1109/JERM.2020.3042696.

[27] S. Shikhantsov *et al.*, “Hybrid Ray-Tracing/FDTD Method for Human Exposure Evaluation of a Massive MIMO Technology in an Industrial Indoor Environment,” *IEEE Access*, vol. 7, pp. 21020–21031, 2019, doi: 10.1109/ACCESS.2019.2897921.



**SILVIA GALLUCCI** received the master's degree in biomedical engineering from the University of Pisa, Italy, in 2019, and the Ph.D. degree in bioengineering from Politecnico di Milano, with a focus on the EMF-human interactions. From January 2024, she currently is a research scientist with the Institute of Electronics, Computer and Telecommunication Engineering, Consiglio Nazionale delle Ricerche. Her current research interest includes the exposure assessment of electromagnetic fields with numerical dosimetry, particularly from 5G mobile communications.



**GABRIELLA TOGNOLA** received the master's degree in Electronic Engineering and the Ph.D. degree in bioengineering, both from Politecnico di Milano, Milan, Italy. She is currently Director of Research with Consiglio Nazionale delle Ricerche, Institute of Electronics, Computer and Telecommunication Engineering. Her main research interests include exposure assessment of electromagnetic fields with numerical dosimetry and with Machine Learning methods and modelling of electromagnetic fields for biomedical applications and innovative EMF applications in connected vehicle.



**MARTINA BENINI** received the B.S. degree in biomedical engineering from Alma Mater Studiorum — Università di Bologna, Italy, in 2017, and the M.S. degree in biomedical engineering from Politecnico di Milano, Italy, in 2020, where she received the Ph.D. degree in bioengineering in 2024. From October 2020 to April 2021, she was a Research Fellow with the Institute of Electronics, Information Engineering and Telecommunications (IEIIT), Consiglio Nazionale delle Ricerche (CNR). Her current research interests include the study of the interaction between the electromagnetic fields (EMFs) and the human body with both deterministic and stochastic dosimetry, with a focus on the antennas used in the automotive field for vehicular connectivity.



**Marta Parazzini** (Member, IEEE) is currently a Senior Researcher with the Institute of Electronics, Computer, and Telecommunication Engineering (IEIIT), Italian National Research Council, Rome, Italy. Her current research interests include the study of the interactions of EMF with biological systems, deterministic and stochastic computational dosimetry, and the medical applications of EMF, in particular the techniques for noninvasive brain stimulation.



**SERENA FIOCCHI** received the master's degree in biomedical engineering and her Ph.D. in bioengineering from the Polytechnic University of Milan, Milan, Italy, in 2009 and 2013, respectively. She currently serves as a Research Scientist at the Institute of Electronics, Computer, and Telecommunication Engineering, National Research Council of Italy, Rome, Italy. Her research interests encompass the study of

the interaction between electromagnetic fields (EMFs) and biological systems with particular focus on the human exposure assessment of EMF, the computational modeling of non-invasive brain and spinal stimulation techniques, as well as on the design and optimization of biomedical technologies utilizing EMFs for diagnostic and therapeutic purposes.